Applied Surface Science Advances 10 (2022) 100262

Contents lists available at ScienceDirect

Applied Surface Science Advances

journal homepage: www.sciencedirect.com/journal/applied-surface-science-advances

The impact of laser-scribing carbon-based supercapacitor electrodes

M. Baptista [a,b,*], G. Gaspar [a], K.G.U. Wijayantha [b,c], K. Lobato [a]

[a] Faculdade de Ciências, Instituto Dom Luiz, Universidade de Lisboa, Lisboa 1749-016, Portugal
[b] Energy Research Laboratory (ERL), Department of Chemistry, Loughborough University, Loughborough LE11 3TU, United Kingdom
[c] Centre of Renewable Energy Systems, Cranfield University, College Road, Cranfield, Bedfordshire MK43 0AL, United Kingdom

ARTICLE INFO

Keywords:
Supercapacitor
Ionic diffusion
Laser scribing
Performance

ABSTRACT

In highly porous carbon electrodes, a large fraction of pores can be inaccessible to the electrolyte, which translates into lower specific capacitances. This is accentuated at high current densities. To circumvent this, channels can be opened to enhance ionic diffusion. In this work, ionic channels were created using a pulsed laser. Nine sets of laser-scribing parameters (pulse fluence and spot spacing) were applied on two sets of carbon-based supercapacitor electrodes: K-bar hand-coated electrodes ("K") and screen-printed electrodes ("SP"). Profilometry and scanning electron microscopy revealed that, before laser-scribing, the latter already had several holes and trenches, whilst the former were compact films. Electrochemical measurements in Na_2SO_4 indicate improvements in the rate capability of the laser-scribed SP electrodes, namely an up to 50% reduction of the rate at which energy density decreases as power densities increase. For laser-scribed K electrodes, the slope of the Ragone plot only decreased by ca. 20% in the best set of conditions. However, for both sets of electrodes, a negative trade-off is observed: laser processed electrodes seem to have a lower specific capacitance. This might be caused by the entrapment of debris in the laser-drilled holes, which could lead to the overestimation of the active mass. Moreover, X-ray Photoelectron Spectroscopy analysis suggests that this may also be explained by the decrease in the oxygen functionalities and by its impact on the electrodes' wettability. On the other hand, for electrodes tested in an organic electrolyte (tetrabutylammonium perchlorate in acetonitrile), the specific capacitance at 2 A/g was up to 66% higher for laser-scribed electrodes and an energy density of 13 Wh/kg was achieved even at 2.8 kW/kg.

1. Introduction

One of the largest challenges for supercapacitors is to increase their energy density without sacrificing their power density nor their cyclability [1]. The energy density of a supercapacitor is proportional to its capacitance and to the square of its stable voltage range [2]. Despite the obvious importance of the latter, the former is perhaps the easier one to tackle and most researchers try to improve this by using pseudocapacitive materials (e.g. MnO_2 and RuO_2) [3] and hybrid configurations (e.g. Li-ion capacitor). However, this trendy strategy often comes at the expense of a reduced cyclability, rate capability [4] and increased cost. Thus, it is reasonable to admit that, in the near future, the industry will continue to favour purely capacitive materials, such as activated carbon (in which the capacitance is proportional to the electrode's accessible surface area) [5].

Another aspect in which the scientific literature greatly diverges from real-world devices is the electrode thickness (which is often much lower than the 200 μm typically used in commercial supercapacitors) [6]. Unlike in literature-reported results, the industry calculates the gravimetric performance based on the whole device (i.e. including the casing, current collector, etc.) [7]. As such, in order to prevent a prohibitively low ratio of active to inactive mass, commercial supercapacitors typically have very high mass loadings (ca. 10 mg/cm^2) [8]. However, in very thick activated carbon electrodes, a significant percentage of the supposedly active mass actually ends up as a "dead weight", since the electrolyte does not efficiently penetrate the electrode's pores, and, consequently, this dead weight does not contribute to the device's capacitance [9]. This effect is particularly relevant at high (dis)charge rates – at lower current densities, the ions are allowed more time to penetrate deeper into the electrode [10].

The accessibility of the electrolyte to the electrode's pores depends on many factors, including the pore size distribution, the size of the solvated ions and the morphology of the electrode [11]. In this sense, a few years ago, templated carbons gained some attention since they

* Corresponding author at: Faculdade de Ciências, Instituto Dom Luiz, Universidade de Lisboa, Lisboa 1749-016, Portugal.
E-mail address: jpbaptista@fc.ul.pt (M. Baptista).

https://doi.org/10.1016/j.apsadv.2022.100262
Received 30 September 2021; Received in revised form 14 May 2022; Accepted 25 May 2022
Available online 6 June 2022
2666-5239/© 2022 The Authors. Published by Elsevier B.V. This is an open access article under the CC BY-NC-ND license (http://creativecommons.org/licenses/by-nc-nd/4.0/).

enabled hierarchical configurations of the pore structure [12]. These promoted access of the electrolyte to the inner parts of the electrode, which translated into an increase in the capacitance [13]. However, the production of templated carbons typically involves long and complex procedures [14], complicating integration in existing mass-production lines.

Lasers are an interesting alternative to tailor the electrode morphology, due to their high efficiency and high speed. Hwang et al. [15] have laser-scribed activated carbon electrodes and demonstrated a fourfold increase in their specific capacitance at high current densities by creating microtrenches that acted as electrolyte "highways" . Their results have motivated a more detailed study on the relationship between laser-processing conditions and their impact on the performance of high mass loading electrodes. The goal is to remove *just enough* mass to increase the electrolyte's accessibility to the inner parts of the electrode without sacrificing a significant amount of active mass and also without compromising the mechanical stability of the electrode. In this work, the laser fluence and the spacing between adjacent channels were varied (in a total of nine different sets of conditions) and the electrochemical performance of the laser-scribed (LS) electrodes in an aqueous electrolyte was compared to that of non-laser-scribed (NLS) electrodes. This study was done on two sets of electrodes: screen-printed electrodes and on K-bar printed electrodes (which had a more compact stacking geometry). Finally, the latter were also tested in an organic electrolyte. This work aims at exploring the feasibility of a simple, cheap and efficient route for obtaining supercapacitor electrodes with a high performance.

2. Experimental

The electrodes were composed of 70 wt.% activated carbon (Norit DLC Supra 50), 20 wt.% of polyvinylidene fluoride (PVDF) (Merck) and 10 wt.% of carbon black (Super C65, TIMCAL). To disperse the components for slurry formation, ca. 2 mL of propylene carbonate (Merck) was added for every gram of the dry mixture. The slurry was further homogenized in a three-roll mill (EXAKT 50 I) and mixed for ca. 20 min at the maximum speed (500 rpm) and at the maximum distance between the rolls (15 μm, this defines maximum particle size). The composition and preparation procedure of the carbon paste was identical for the two different sets of electrodes.

For the first set (henceforth referred as "SP"), several squared electrodes with an area of 1 cm^2 were fabricated with an automated screen-printer (ATMA, AT-45PA), using stainless steel as the substrate (Hollinbrow Precision Products, 25 cm × 30 cm, 50 μm-thick, grade 1.4310/301/$X_{10}CrNi_{18-8}$/$X_{12}CrNi_{17-7}$). This technique (schematised in Fig. 1) permits the fast production of a large number of electrodes with well-defined areas and similar thicknesses.

The screen (SAATI, PE AM 36.90PW) had a 190 μm mesh opening, 90 μm of nominal thread diameter and the theoretical thickness of the wet film is almost twice this value (ca. 150 μm). However, the resultant thickness of the deposited film after drying is obviously lower and depends on the slurry's solvent content. To obtain thicker electrodes, two layers were printed on top of each other. Between the consecutive prints, the electrodes were dried in the oven at 120° C for 10 min. After the second print, the electrodes were dried for ca. 12 h in the oven at 120° C. Finally, individual electrodes were formed by manual cutting of the screen-printed sheets.[1]

The second set of electrodes (henceforth referred as "K") were hand-printed with a 100 μm[2] K-bar on top of stainless steel sheets identical to the ones used in the first set. To obtain thicker electrodes, two layers were printed on top of each other. Between the consecutive prints, the electrodes were dried in the oven at 120° C for 10 min. After the second print, the electrodes were dried for ca. 12 h in the oven at 120° C. Finally individual 0.5 cm^2 electrodes were hand-cut.

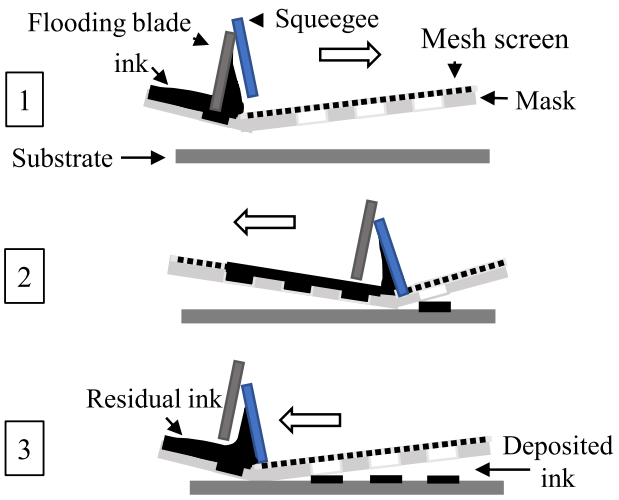


Fig. 1. Printing process. (1) The flooding blade moves slightly downwards and starts moving rightwards, spreading the ink onto the mesh; during this step, the screen never touches the substrate; (2) When the whole mesh is already flooded, the squeegee moves downwards and starts moving leftwards, pushing the ink out of the screen and onto the substrate; (3) As the squeegee keeps moving forward and depositing the ink on the substrate, the residual ink is collected to be reused in the next print.

Electrodes were then subjected to a preliminary electrochemical characterization (as described below) and then carefully washed with deionized water and dried. Based on these preliminary measurements, their capacitances were calculated, and the electrodes were distributed in groups of 5. Each group was composed to maximize the standard deviation amongst the capacitances of its elements while ensuring that their average capacitance was as similar as possible to that of other groups. In total, 10 groups were constituted: one had non-laser-scribed electrodes (NLS) and the other groups were laser-scribed with a 1064 nm Nd:YAG pulsed laser (SPI Lasers, G3.1 SM Series), with a S4LFT0202/094 f-Theta Lens coupled to a Raylase galvano head with 2-axis subsystems for laser beam deflection, using a pulse width of 45 ns, 9 different combinations of three pulse energies and three interchannel spacings: (257 μJ, 100 μm); (314 μJ, 100 μm); (371 μJ, 100 μm); (257 μJ, 120 μm); (314 μJ, 120 μm); (371 μJ, 120 μm); (257 μJ, 140 μm); (314 μJ, 140 μm); (371 μJ, 140 μm). The laser spot's full-width-half-maximum was ca 40 μm. The channels were equidistantly drilled, according to the pattern depicted in Fig. 2. In the K set, some electrodes were also scribed with the maximum available pulse energy (571 μJ) and a 140 μm spacing. Others were scribed at 257 μJ, but scanned at a much lower speed (1104 mm/s), to form continuous trenches (with a 140 μm distance between parallel lines) instead of individual holes.

Micrographs of the samples' surface were acquired using a field

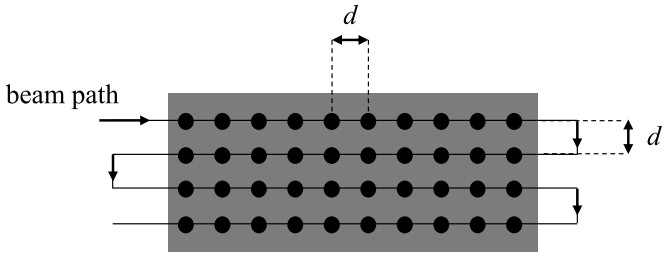


Fig. 2. Laser-scribing pattern with equidistant channels. d is the interchannel spacing. For $d = 100$ μm, the irradiated area is ca. 13%; for $d = 120$ μm, the irradiated area is 9% and for $d = 140$ μm it is 6%.

[1] A portion of the coated stainless steel was left bare to enable the connection to a crocodile clip for 3-electrode electrochemical measurements.

[2] Wet film thickness

emission scanning electron microscope (SEM) model JEOL JSM-7001F at an accelerating voltage of 15 kV.

For set SP, profilometry measurements have been performed with an InfiniteFocus G5 plus (Bruker Alicona) at a 10x magnification with a lateral resolution of ca. 1 μm. The raw data was plane levelled, and the images generated using Gwyddion software (version 2.59). For set K, a Sensofar S neox non-contact 3D optical profiler (software version 6.2.0.0) was used under focus variation imaging mode. A 10x lens was also used, enabling maps with an area of 1747×1313 μm^2 and lateral resolution of ca. 1 μm.

The surface compositions of the reference NLS and the 314 μJ laser-scribed samples were measured through X-ray Photoelectron Spectroscopy (XPS) analysis using a Thermo Scientific K-Alpha X-ray Photoelectron Spectrometer equipped with a monochromatic Al Kα X-ray source. The excitation sampling spot size was 400 μm, and the high-resolution spectra were collected with 0.1 eV spectral resolution. The spectra were deconvoluted using the Avantage software while the elemental concentration quantification was applied using standard single element sensitivity factors.

To probe the chemical composition of the carbon-based material developed in this work, Raman spectra were measured using a Jobin Yvon HR800 (Horiba, Japan) apparatus fitted with a 442 nm He-Cd laser line (Kimmon IK Series, Japan). The laser light was focused on the samples by using a 50x (0.7 NA) objective lens that resulted in a spot analysis of ca. 1 μm in diameter, while the Raman signal is collected by a multichannel CCD detector. Here, each spectrum was collected using a total acquisition time of 30 s. In the SP set, no well-defined laser craters were visualized during Raman inspection, and thus, for these samples, a total of three spots were randomly measured throughout the sample surface. Since laser induced craters in the K set were clearly identified, it was possible to probe their periphery as well as their inner areas. A total of 3–4 craters were measured for these samples.

The baseline of all spectra was removed using a 4th degree polynomial fit, and the corresponding bands identified and deconvoluted using LabSpec software.

The electrochemical measurements have been performed with an Autolab PGSTAT302N (Metrohm) operated with NOVA 2.1 software. The electrodes were submerged in aqueous solutions of Na_2SO_4 (1 M), in a 3-electrode setup using a Ag|AgCl (3 M) reference electrode and a mixed metal oxide-coated titanium counter electrode (De Nora). In the working electrode, the stainless steel substrate was masked with Kapton tape to prevent its direct contact with the electrolyte. All the electrochemical measurements initiated with 60 wetting cycles performed at 30 mV/s between −0.4 V and 0.5 V. Next, the electrodes were tested within this same range at varying scan rates (10, 20, 40, 50, 60 and 75 mV/s) and then galvanostatic charge-discharge tests were carried out (also from −0.4 V to 0.5 V) at several current densities (1–8 mA/cm^2). Only the 10th voltammogram/charge-discharge cycle was considered for calculations. Finally, the electrodes were also characterized by potentiostatic electrochemical impedance spectroscopy, at open circuit potential with a 10 mV amplitude, from 500 kHz to 40 mHz. For the measurements carried out in 0.2 M of tetrabutylammonium perchlorate (TBAP) in acetonitrile, a silver wire was used as a pseudo-reference and a 1 cm^2 Pt plate was used as the counter electrode. The measurements were carried out between −1 V and 1 V vs Ag pseudo-reference.

The specific capacitance (C_{sp}), the energy density (E_{sp}) and power density (P_{sp}) during discharge were calculated, respectively, via Eqs. (1)–(3):

$$C_{sp}[\mathrm{F/g}] = \frac{i\,(t_f - t_0)}{[V(t_f) - V(t_0)]m} \quad (1)$$

$$E_{sp}[\mathrm{Wh/kg}] = \frac{0.5\ C_{sp}\ [V(t_f)\ - V(t_0)]^2}{3.6} \quad (2)$$

$$P_{sp}\ [\mathrm{kW/kg}]\ = \frac{3.6\ E_{sp}}{t_f - t_0} \quad (3)$$

where, t_0 and t_f are, respectively, the time at the start and end of the discharge, i is the (constant) value of the current, $V(t_f)$ and $V(t_0)$ are, respectively, the potential at the end and at the start (i.e., after the initial IR drop) of the discharge, and m is the electrode mass (in g).

Symmetric CR2032 coin cells (16 mm electrode diameter) soaked in 1 M Na_2SO_4 aq were measured with an Autolab PGSTAT302N (Metrohm) operated with NOVA 2.1 software, between 0 and 0.9 V, using a procedure identical to the one described above. The cyclability measurements have been performed with a BTS4000–5V10mA battery tester (Neware), where the cells were tested for 10,000 cycles at 2 mA/cm^2. The presented results correspond to average of 5 samples from each group set.

To determine the active mass of the electrodes, these were carefully rinsed with deionized water, dried and weighed. Subsequentially, the active electrode material was removed, and the current collector was also weighed. The electrode mass is the difference between the measured masses before and after the removal of the electrode active material. The average mass loading was found to be 5.1 ± 0.7 mg/cm^2 (1 σ).

3. Results and discussion

3.1. Morphology

Fig. 3a) shows that, prior to laser-scribing, the SP electrodes already contained some trenches due to their fabrication method. A thin grid was placed on top of the topographical images to assist the visualization of the marks left by the screen. In Fig. 3(b)−(d), in addition to the screen mesh, some laser-drilled channels are also visible. These figures show two different patterns, which are superimposed. However, it was impossible to control the type of superposition, namely the exact trench orientation resultant from the screen's mesh, and the alignment between these trenches and the laser-scribed pattern. The result is that some channels were created within the trenches, others not, and others on the slopes of the trenches. In these trenches, the effect of the laser is obviously less important due to the low local thickness of the film. In Fig. 4, the grey scale enables an easier identification of surface changes induced by the laser (b), but it also demonstrates the existence of a high macroporosity in the NLS electrode (a). Figs. 5 and 6 show that K electrodes were considerably smoother before irradiation, hence enabling a clear identification of the laser-scribed pattern. As the pulse energy increases, the channels tend to get wider and deeper. However, even when the maximum available pulse energy (571 μJ) is used, the maximum depth is between 60 and 70 μm (only roughly half the electrode's thickness), as demonstrated in Fig. 5(d) and in Fig. 6(f). As the laser beam travels through the highly opaque electrode, it is quickly absorbed, its fluence decreases and, consequently its "ablation ability" as well. As a result, the channels are not as deep as intended. Another possible explanation is that the apparent bottom of the channel is partially composed of trapped debris – this would lead to an underestimation of the lost mass (and thus to an overestimation of the active mass).

Fig. 7 shows that, for most sets of conditions, the percentage of lost mass is typically 5–10%. For a 40 μm spot size and a 100 μm spacing, the fraction of irradiated area is ca. 13% and thus the measured mass losses appear reasonable (which does not exclude the possibility of existing trapped debris). For a pulse energy of 571 μJ, the lost mass is about the same as the one recorded for the trenched pattern (ca. 16%).

3.2. Electrochemistry

3.2.1. Screen-printed electrodes

Fig. 8(a)−(c) show that, as the scan rate increases, the laser-scribed

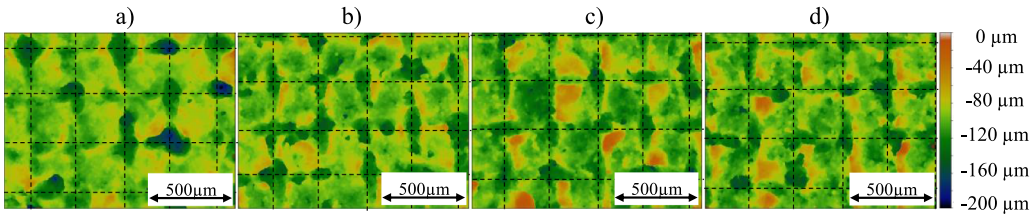


Fig. 3. Profilometry measurements performed in (a) non-laser-scribed electrode ; (b) laser-scribed at 314 µJ with an interchannel spacing of (b) 140 µm; (c) 120 µm; and d) 100 µm. In (a) some trenches are already visible due to screen-printing. The grid represents the trenches resultant from the screen's mesh.

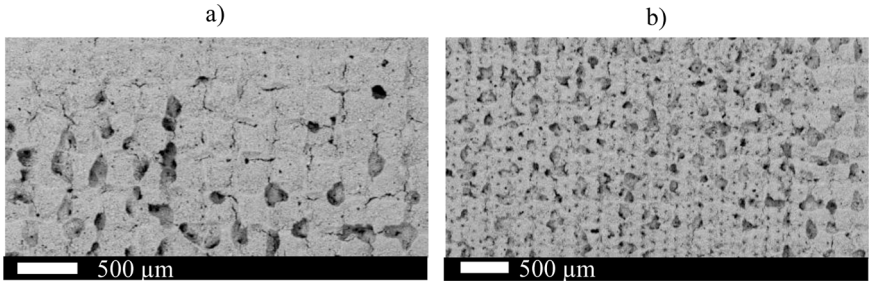


Fig. 4. Stitched micrographs at low magnification of a screen-printed (a) non laser-scribed electrode and (b) an electrode laser-scribed with a 140 µm spacing (b).

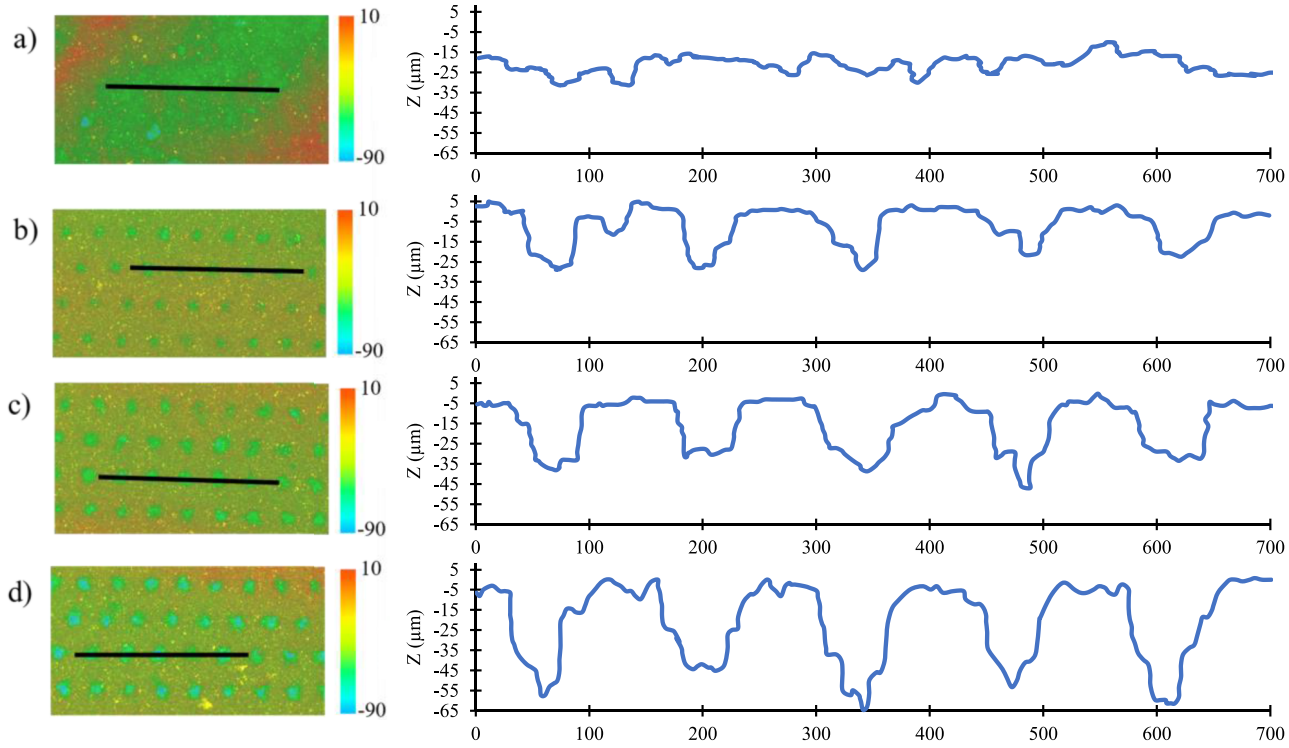


Fig. 5. Profilometry measurements of (a) non laser-scribed electrode and electrodes laser-scribed with a 140 µm spacing and (b) 257 µJ, (c) 371 µJ and (d) 571 µJ (K set).

electrodes manage to retain a more rectangular shape when compared to NLS ones, which suggests facilitated ionic diffusion. Fig. 8(d) aims to quantify this observation by comparing the "fill factors" (*FF*) of the voltammograms obtained for LS and NLS electrodes at increasing scan rates. *FF* is defined by Eq. (4):

$$FF = \frac{\int_{t_0}^{t_f} i(t)dV(t)}{\Delta V(i_{max} - i_{min})} \quad (4)$$

where t_0 and t_f are, respectively, the instant when the cycle begins and when it finishes; i is the instantaneous current and dV is the step in the potential (which depends on the scan rate and which is positive in the forward sweep and negative in the backwards sweep); ΔV is the difference between the maximum and the minimum potentials and i_{max} and i_{min} are, respectively the maximum and the minimum currents recorded during the cyclic voltammetry.

Fig. 9 shows that, at low current densities, the (dis)charge time is ca. 25% shorter for the LS electrodes, meaning that the areal capacitance is smaller than that of NLS. This is probably due to the fact that, at low current densities, the ionic diffusion in NLS electrodes is sufficient to

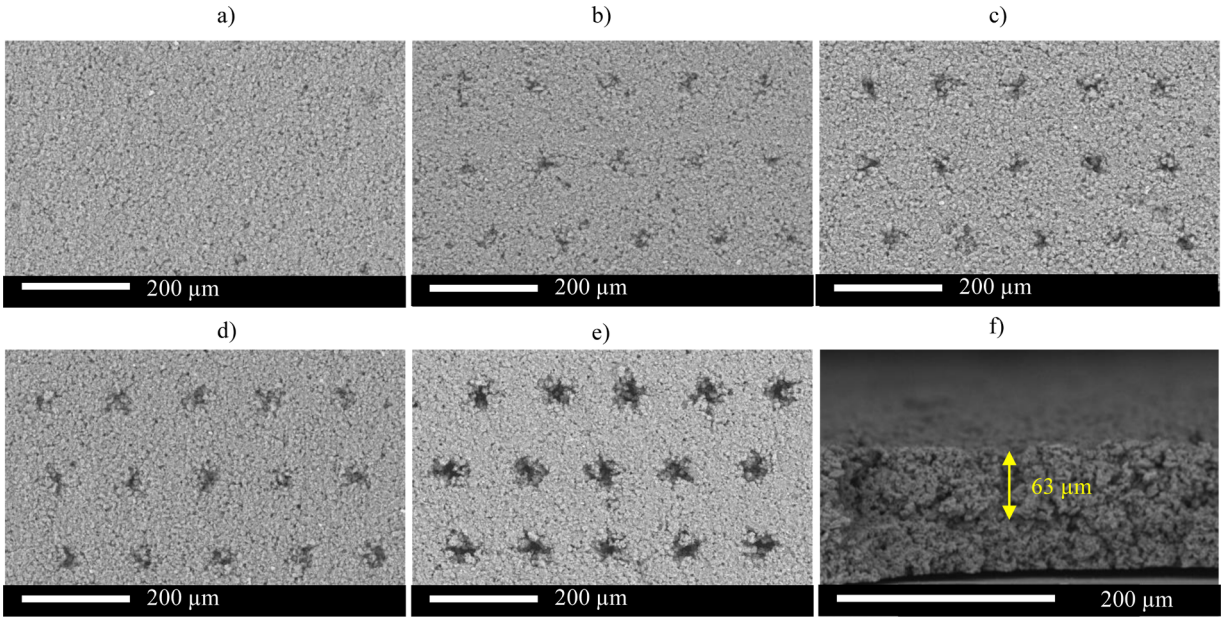


Fig. 6. K-bar set: micrographs taken at a 710x magnification of (a) non laser-scribed electrode and electrodes laser-scribed with a 140 µm spacing and 257 µJ, 314 µJ, 371 µJ and 571 µJ (b, c, d and e, respectively); (f) Cross-sectional micrograph (1433x) demonstrating the depth of holes in laser-scribed electrode identical to the one shown in (e).

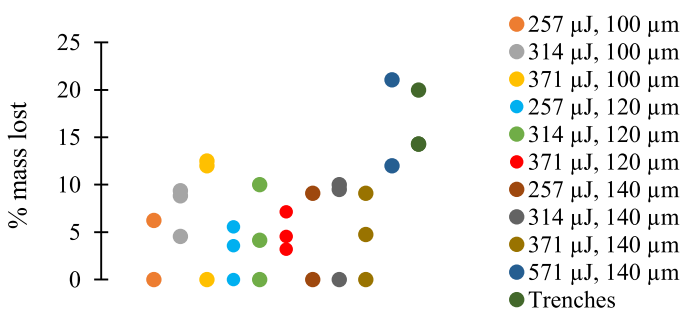


Fig. 7. Percentage of electrode mass lost upon laser-scribing with each set of conditions (K-bar set).

enable access to the inner pores. Since, in these conditions, practically all the surface area is available to the electrolyte, the removal of active mass leads to a capacitance decrease. As the current density increases, the ohmic drops of both the NLS and LS electrodes increase, but that of LS electrodes is always lower, as shown in Table 1.

As shown in Fig. 10, all the sets of laser-scribing conditions resulted, on average, in Ragone plots with lower slopes than the non-laser-scribed electrodes. There is, however, an unexpected caveat: the fact that, at low power densities, the energy density is always lower for the laser-scribed electrodes. As explained earlier, one expects to obtain lower absolute capacitances at low power densities due to the removal of active material. However, when normalized by the electrodes' masses (for each electrode, its mass was determined after the measurements, as detailed above), this effect should no longer be visible – i.e., at low power densities, the energy density of NLS and LS electrodes was expected to be the same. The energy density is proportional to the specific capacitance and to the square of the operational range of potentials and, as such, to understand this behaviour, those two variables were plotted separately versus power density, as shown in Fig. 10, together with the electrodes' rate capability (Fig. 11a).

Fig. 11(b) shows that, for the LS electrodes, although the specific capacitance decreases more slowly with increasing power densities, it is always lower than that of NLS electrodes. At the same time, due to a decrease in the ohmic losses, the operational ΔV is always higher for the LS electrodes and this difference becomes accentuated at higher power densities (Fig. 11c)).

Fig. 11 only shows the comparison between NLS electrodes and electrodes laser-scribed @ 314µJ, with an interchannel spacing of 100 µm and 140 µm, but similar behaviours were found for the other laser-scribing conditions. This suggests a trade-off between specific capacitance and ΔV which explains the trends observed in Fig. 11: at low power densities, the voltage drop is negligible and thus, since the NLS electrodes have a higher specific capacitance, their energy density is higher; at high rates, the voltage drop is more significant and there is a smaller difference between the specific capacitances of LS and NLS electrodes, which causes the energy density to be higher in laser-scribed electrodes. However, this only happens for very high-power densities and, for some sets of laser-scribing conditions, it does not happen at all (or at least not within the range of tested power densities). The set of electrodes laser-scribed @ 314 µJ with a 140 µm interchannel spacing demonstrate the more promising results as their energy density starts exceeding that of non-laser-scribed electrodes at lower power densities (>250 W/kg). This is mainly attributed to their greater average specific capacitance (although still lower than that of NLS electrodes). It is worth stressing that, for an interchannel spacing of 140 µm, the number of channels per unit area (5102 cm^{-2}) is approximately 50% of the value obtained when a 100 µm interchannel spacing is employed (10,000 cm^{-2}). Despite the absence of a clear trend (most likely due to the pre-existing trenches), the data seems to suggest that a lower areal density of channels is more beneficial to the overall performance.

Fig. 12 shows noticeable differences between the Nyquist plots of the LS and NLS electrodes. An equivalent electric circuit (shown as an inset) was fitted to the data. One of the most important parameters to investigate mass transfer limitations is the Warburg coefficient (W), which relates to the diffusion coefficient by Eq. (5) [16]:

$$W = \frac{RT}{n^2F^2A\sqrt{2}}\left(\frac{1}{\sqrt{D}\,C^*}\right) \quad (5)$$

where R is the gas constant, T is the absolute temperature, n is the charge-transfer number, F is the Faraday constant, A is the area of the electrode's surface, D is the diffusion coefficient, and C^* is the electrolyte concentration.

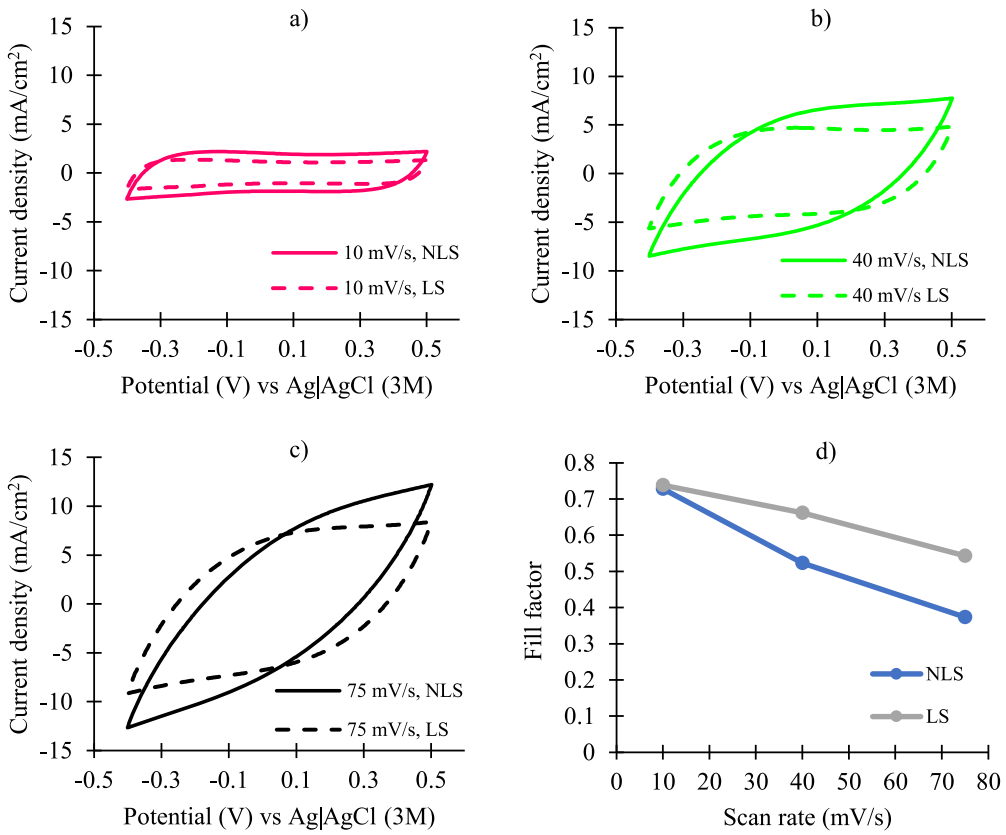


Fig. 8. Average voltammograms of cyclic voltammetries performed in screen-printed laser-scribed (LS) and non laser-scribed (NLS) electrodes at (a) 10 mV/s, (b) 40 mV/s, (c) 75 mV/s and (d) "Fill factors" obtained for LS and for NLS electrodes at different scan rates.

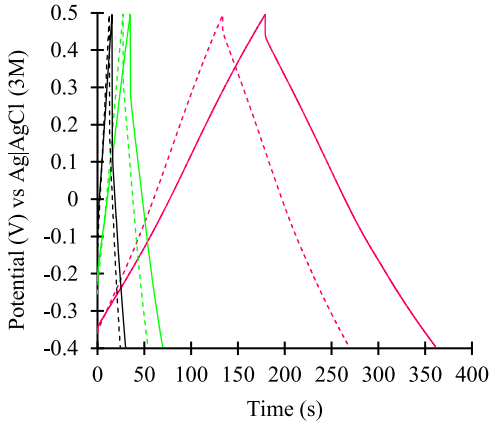


Fig. 9. Galvanostatic charge-discharge plots obtained at 1 mA/cm^2 (pink), 4 mA/cm^2 (green) and 8 mA/cm^2 (black) for screen-printed non laser-scribed (solid lines) and laser-scribed (LS) electrodes (broken lines) with 314 μJ pulse energy and 100 μm interchannel spacing (broken lines).

Table 1
Voltage drops (in mV) obtained at different current densities for non-laser-scribed (NLS) electrodes and for electrodes laser-scribed with a pulse energy of 314 μJ and an interchannel space of 100 μm (LS).

	Discharge time (s)		IR drop (mV)	
	NLS	LS	NLS	LS
1 mA/cm^2	182	135	54	47
4 mA/cm^2	34	26	196	173
8 mA/cm^2	14	11	335	301

Table 2
Simulated parameters obtained for the equivalent electric circuits corresponding to the non-laser-scribed electrode and electrode laser-scribed at 314 μJ and an interchannel space of 100 μm (LS) – SP set.

	NLS	LS
R_1 (Ω)	5.7	7.5
R_2 (Ω)	14.6	11.6
R_3 (Ω)	8.3	6.0
CPE (s^N/Ω)	7.5×10^{-5}	7.9×10^{-5}
N	0.74	0.75
W ($\Omega/\sqrt{s}$)	15.1	12.4
C (mF)	209	134

To apply this equation requires knowledge of the electrode's surface area. However, since W is inversely proportional to $\sqrt{D}$, a lower Warburg coefficient translates into a higher diffusion coefficient. The Warburg coefficient was found to be 15.1 $\Omega/\sqrt{s}$ for the NLS electrode and 12.4 $\Omega/\sqrt{s}$ for the LS electrode, indicating a higher diffusion coefficient for the latter.

To investigate if the preliminary 3-electrode results held true for complete devices, cells were fabricated with LS and NLS electrodes. Fig. 13(a) shows that, despite a modest performance, the average slope of the Ragone plot obtained for the LS cells is lower than that obtained for the NLS cells. More importantly, at 80 W/kg, the LS cells managed to maintain an energy density twice as high as the NLS cells tested at the same rate. Fig. 13(b) shows that the laser-scribing does not affect the cyclability, since the capacitance retention after 10,000 cycles is essentially the same for the LS and for the NLS cells.

Despite these promising results, the pre-existing trenches of the electrodes make the results uncertain and preclude the establishment of a clear trend amongst the various sets of conditions. Section 3.2.2. presents the electrochemistry results obtained for the K-bar electrodes.

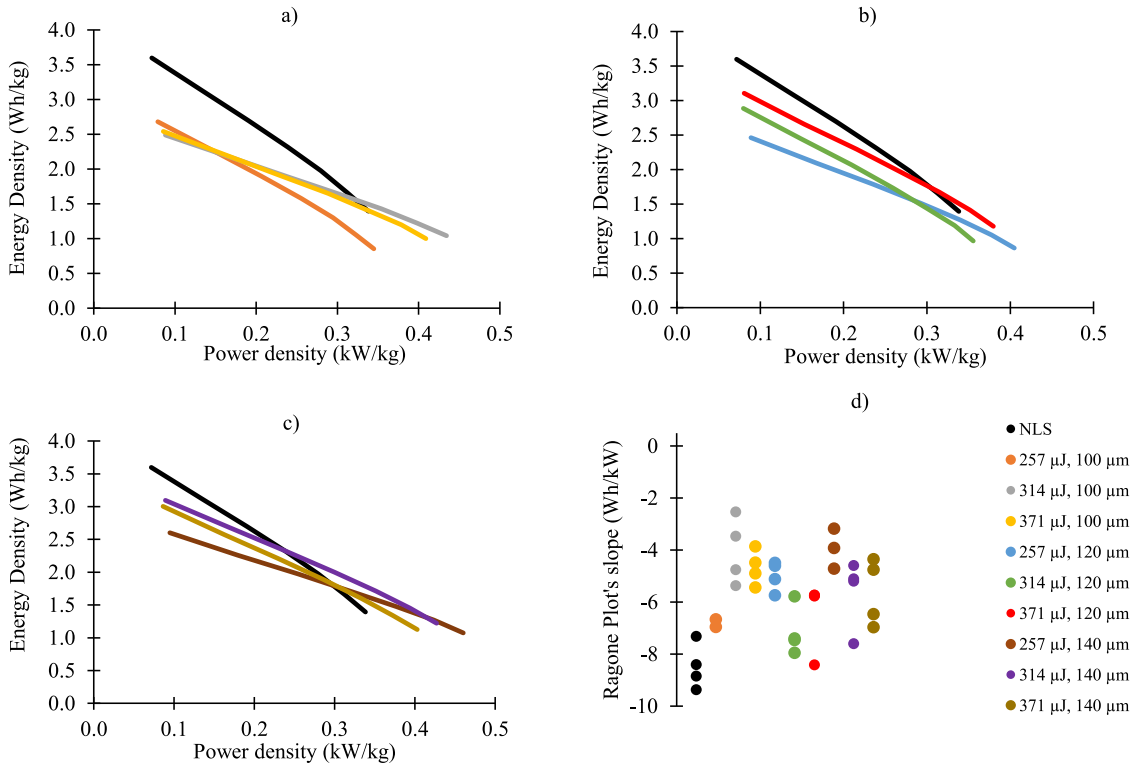


Fig. 10. Average Ragone plots obtained for screen-printed non laser-scribed (NLS) electrodes and for electrodes processed with the 3 different pulse energies and interchannel spacing of (a) 100 µm, (b) 120 µm and (c) 140 µm; (d) shows the spread of the values obtained for the slopes of the Ragone plots of individual electrodes belonging to the non laser-scribed (NLS) group and to the 9 laser-scribed groups.

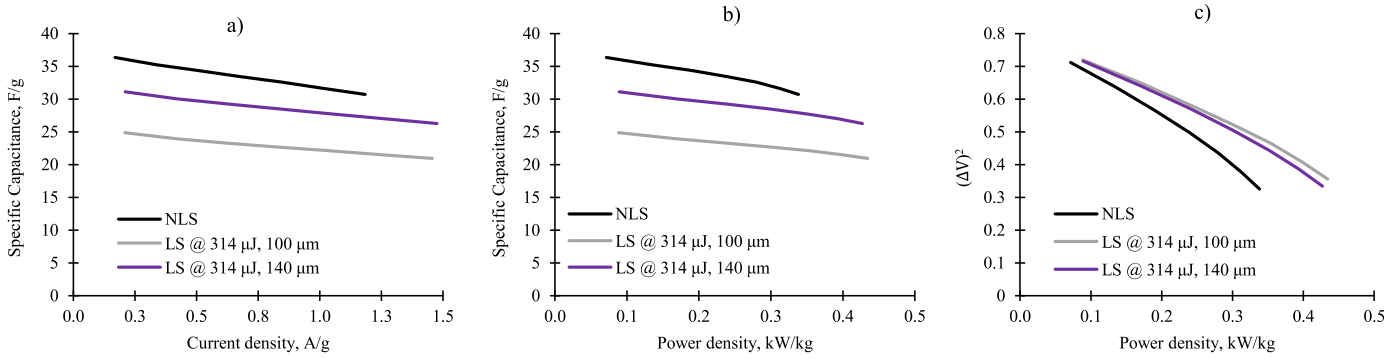


Fig. 11. Average evolution of specific capacitance with current density (a) and with power density (b) and the square of the operational ΔV (c) with current density for screen-printed non laser-scribed (NLS) and for laser-scribed (LS) electrodes @ 314µJ with an interchannel spacing of 100 µm and 140 µm.

3.2.2. *K-bar electrodes*

To enhance the behaviour at diffusion-limited conditions, these measurements were performed for wider current ranges. The same was not done in the previous section to prevent potential damage to the electrodes (not brought on directly by the high currents, but by an eventual overpotential, in case the high currents caused the electrodes to overcharge too fast hence evading the instrument's cut-off mechanism). Yet, given the importance of comparing the rate capability of the electrodes in this study, the electrodes were tested up to almost 4 A/g. Fig. 14 (a–c) shows the Ragone plots obtained for the K electrodes laser-scribed under the various conditions and Fig. 14d) shows the slopes obtained for these plots at high current densities. Similarly to Fig. 10, Fig. 14 also suggests that larger interchannel distances (i.e. a lower areal density of holes), is more advantageous than shorter distances. Yet, even for the best conditions (which seem to be for electrodes laser-scribed either with trenches or with 571 µJ and a 140 µm spacing), the slopes of the Ragone plots only decrease by ca. 20% when compared to NLS electrodes

Fig. 15 shows that, for the best conditions, the specific capacitance is essentially the same as that of NLS electrodes (for the other conditions, the specific capacitances are lower than the reference's).

Fig. 16 and Table 3 reveal that the Warburg coefficients of the LS electrodes are lower (11.1 $\Omega/\sqrt{s}$ for the electrode processed with 571 µJ and 7.5 $\Omega/\sqrt{s}$ for the electrode laser-scribed with trenches) than that of the NLS electrode (16.5 $\Omega/\sqrt{s}$), which suggests an improved ionic diffusion. However, this positive effect seems to be counterbalanced by another factor that renders the overall impact negligible.

These results suggest that the ionic diffusion at high currents is not a significant limitation for these electrodes when tested in Na_2SO_4. Indeed, it is widely known that the solvated radii tend to be considerably larger in organic than in aqueous electrolytes and thus the diffusion-related limitations should be more evident. Fig. 17 shows that, in 0.2 M of TBAP (in acetonitrile), the performance is visibly improved in LS

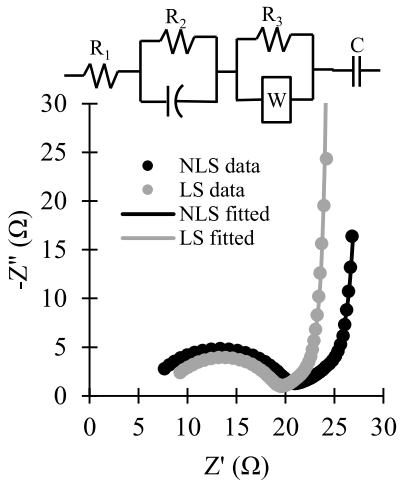


Fig. 12. Nyquist plots obtained for screen-printed non laser-scribed (NLS) (black dots) and laser-scribed (LS) electrodes (grey dots) at 0 V vs AglAgCl (3 M), their respective fits (solid lines) to the equivalent electric shown. R_1 is the contact resistance, R_2 is the charge transfer resistance and the constant phase element (CPE) represents the admittance of the double layer (the higher the associated N value, the more similar it is to a perfect capacitor), R_3 and the Warburg component represent the impedance associated to the ionic diffusion within the electrode and C is the absolute capacitance of the electrode. Fitting parameters can be found in Table 2.

electrodes. For example, at 2 A/g the specific capacitance was up to 66% higher for laser-scribed and an energy density of 13 Wh/kg was achieved even at 2.8 kW/kg.

3.3. Surface composition

A possible explanation for the detrimental effect of the laser on the specific capacitance is the alteration of the surface chemistry. Indeed, in addition to the morphological changes, it is also important to consider the impact of subjecting the material to highly energetic pulses. In the formation of the channel, parts of irradiated surface are vaporized, while the adjacent material (activated carbon, carbon black and binder) suffers considerable heating which can translate into the chemical transformation of the surface of the channels [17]. For example, assuming a 40 μm spot diameter, a 314 μJ pulse results in a local irradiation of 25 J/cm^2 - this is the same order of magnitude of fluence values which have been reported to induce a local graphitization of amorphous carbon films [18]. XPS and Raman measurements can provide useful information on this.

3.3.1. XPS

In Fig. 18a), the deconvoluted C1s peaks seem to be almost identical for the non-laser-scribed (NLS) and laser-scribed (LS) electrodes. However, peak fitting is not always a straightforward task and thus some subtle differences - particularly regarding the relative importance of graphitic and diamond-like bonds - might be unclear [19]. In amorphous carbons (such as activated carbon), there is usually a mixture of these two types of peaks and the best way to identify the preferential hybridization is with the D parameter [20]. This parameter is basically the difference between the binding energies corresponding to the maximum and the minimum of the first derivative of carbon's Auger peak [21]. Diamond-like materials (mainly sp3) typically have a D parameter of 11–13 eV whilst graphite (mainly sp2) has a D parameter of 21–23.0 eV [22]. Based on the plots of the differentiated CKL1 peaks obtained for the NLS and LS samples (Fig. 18b)), the D values were found to be 18.9 eV and 19.4 eV, respectively. This suggests that the laser might have induced a partial graphitization of the sample - an effect that has already been described in the literature [23]. However, since the increase in D is small, this change should be interpreted cautiously and with the assistance of complementary techniques. Also, it is worth stressing that the XPS data presented here were acquired for a relatively large spot diameter (400 μm) and thus include both laser-scribed and non-laser-scribed regions (for an interchannel distance of 100 μm and assuming a 40 μm laser spot diameter, the fraction of irradiated area is only ca. 13%). Moreover, since this technique is highly superficial (it only describes the first few nanometres of the surface), the signal coming from the laser-scribed regions is expected to be smaller compared to that of the non-laser-scribed regions. Most of the detectable chemical changes will be from the borders of the channels. Although the energy of the laser pulse decreases with the penetration depth (due to absorption), it is still reasonable to admit that the results provided by XPS underestimate the effect of the laser (i.e., if greater depths were visible, the differences between LS and NLS would be more striking). Yet, it is very clear that, as expected, the laser had an impact on the binder (PVDF), as shown by the smaller size and slight shift in the F1s peak (Fig. 18c)). Also noteworthy is the reduced size of the O1s C—O and C = O peaks obtained for the laser-scribed sample (Fig. 18d)), suggesting that the oxygen functionalities have been significantly affected. These functional groups are known to contribute to capacitance by promoting fast and

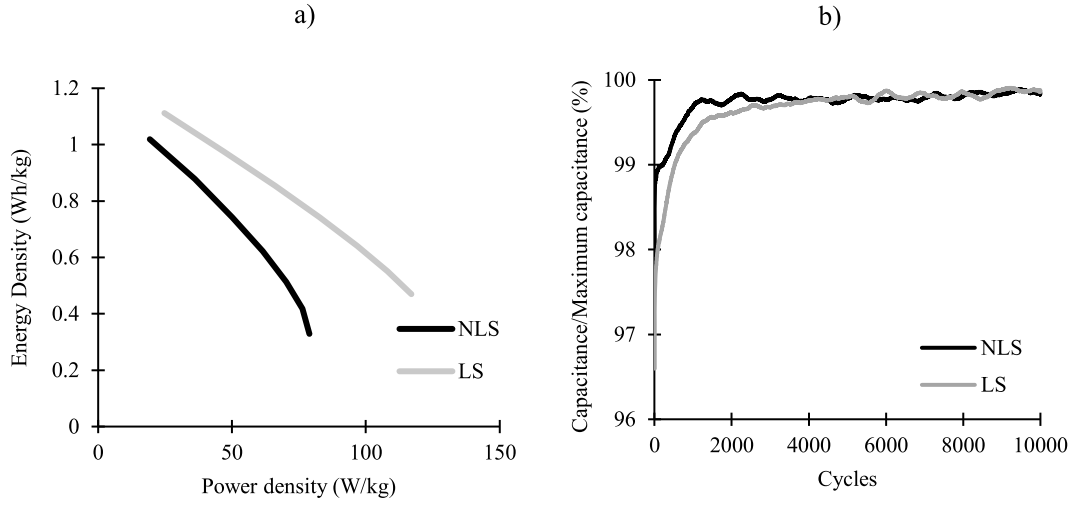


Fig. 13. (a) Average Ragone plots obtained for cells fabricated with non laser-scribed (NLS) electrodes and with laser-scribed (LS) electrodes; (b) Average evolution of the ratio between the capacitance and the maximum capacitance along 10,000 charge-discharge cycles in symmetric coin cells (LS and NLS) cycled at ca. 2 mA/cm^2. These results were smoothed with a moving average of 100 elements.

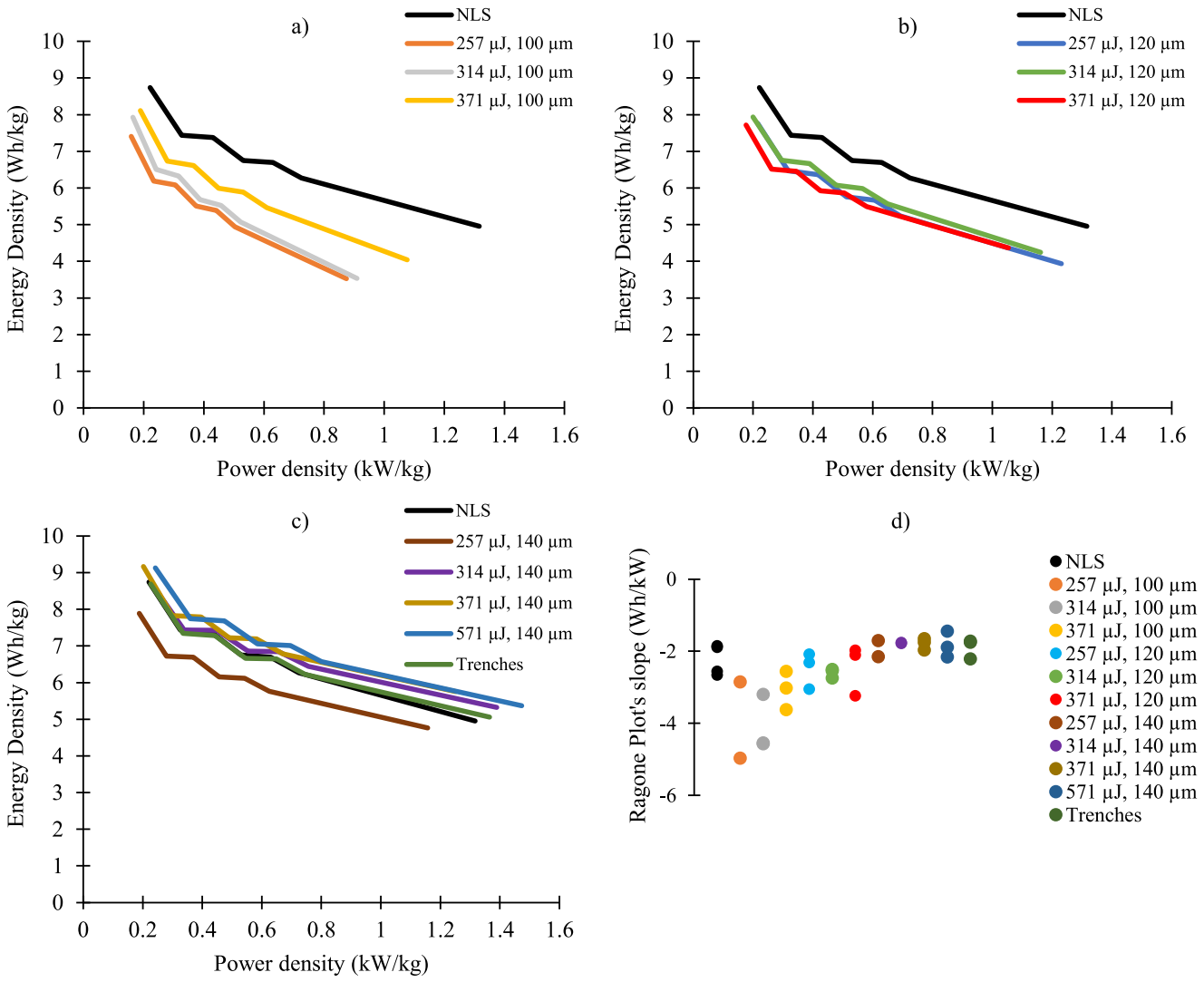


Fig. 14. Average Ragone plots obtained for non laser-scribed (NLS) electrodes and for electrodes processed with the 3 different pulse energies and interchannel spacing of (a) 100 µm, (b) 120 µm and (c) 140 µm; (d) shows the spread of the values obtained for the slopes of the Ragone plots of individual electrodes belonging to the NLS group and to the 9 laser-scribed groups (K-bar set). Slopes calculated between 1.6 A/g and 3.2 A/g, by least squares fitting.

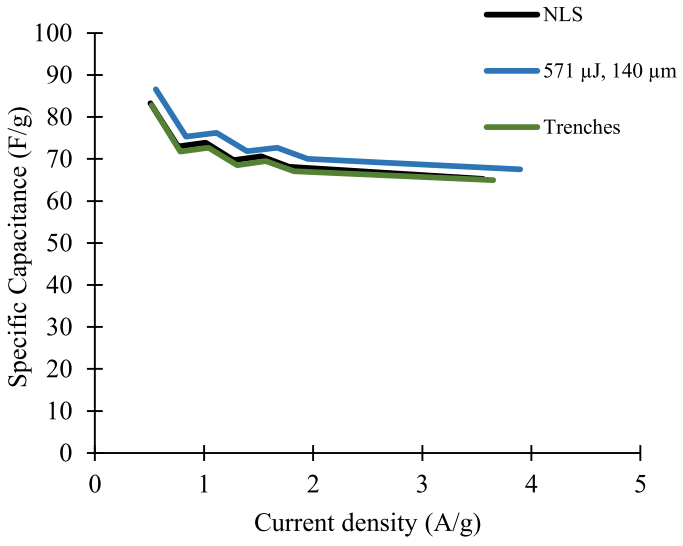


Fig. 15. Average rate capability of non laser-scribed (NLS) and laser-scribed electrodes.

reversible faradaic reactions [24] and also by enhancing the wettability of the electrode [25,26] and thus their decrease could partially account for the observed performance loss.

Fig. 19 complements the information provided in Fig. 18, by presenting the relative abundance of the as-described bonds. In general, there seems to be an increase in the carbon content and a decrease in the oxygen and fluorine content, as expected. Table 4 shows that most of the peak positions and shapes remained essentially unaltered. The only noteworthy exceptions are the O1s O-Fx and the F1s peaks (which suffered a −0.4 eV and a −0.2 eV shifts after processing).

3.3.2. *Raman spectroscopy*

Fig. 20 shows representative Raman spectra for screen-printed electrodes under NLS and LS (314 µJ and 100 µm) conditions. The spectra are represented for a Raman shift range from 1100 to 3200 cm^{-1}. The D-band and G-band are clearly identified in both spectra, having comparable intensities. The D-band at 1364 cm^{-1} is related to lattice defects and low symmetry in the carbon structure while the G-band at 1587 cm^{-1} is usually attributed to a characteristic first-order mode of graphite and stretching of C = C bonds [27]. The degree of graphitization of a certain carbon material can be obtained from the ratio between D-band and G-band peak intensities (I_D/I_G), where a higher degree of

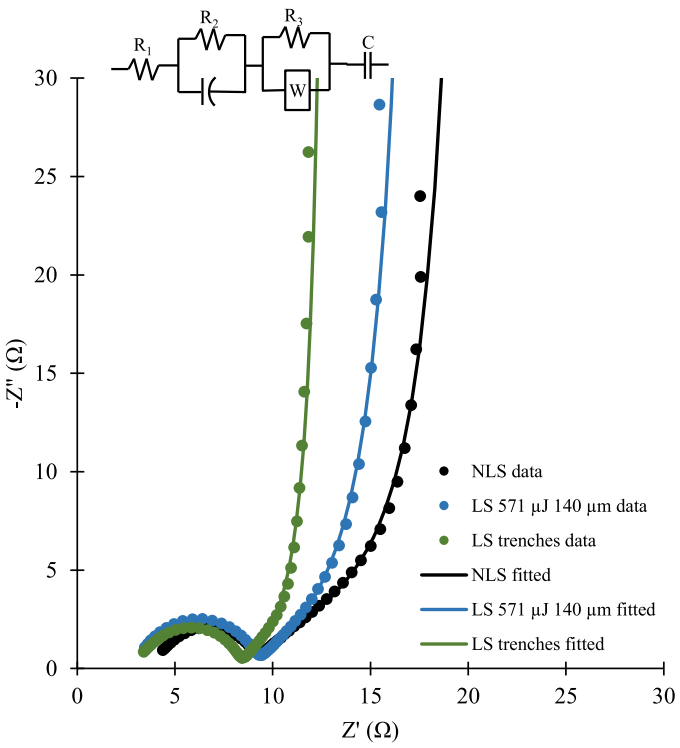


Fig. 16. Nyquist plots obtained for non laser-scribed (NLS) and for laser-scribed (LS) electrodes at 0 V vs AglAgCl (3 M) and their respective fits to the equivalent electric circuit shown. R_1 is the contact resistance, R_2 is the charge transfer resistance and the constant phase element (CPE) represents the admittance of the double layer (the higher the associated N value, the more similar it is to a perfect capacitor), R_3 and the Warburg component represent the impedance associated to the ionic diffusion within the electrode and C is the absolute capacitance of the electrode. Fitting parameters can be found in Table 3.

Table 3
Simulated parameters obtained for the equivalent electric circuits corresponding to the non-laser-scribed (NLS) electrode and laser-scribed (LS) electrodes (571 µJ 140 µm and trenches) – K set.

	NLS	LS 571 µJ 140 µm	LS trenches
R_1 (Ω)	4.0	3.0	3.1
R_2 (Ω)	4.8	5.9	5.1
R_3 (Ω)	13.3	10.5	5.5
CPE (s^N/Ω)	8.7×10^{-5}	6.2×10^{-5}	12.5×10^{-5}
N	0.86	0.87	0.83
W ($\Omega/\sqrt{s}$)	16.5	11.1	7.5
C (mF)	143	118	120

graphitization material should present a low ratio (typically below 1). Here, the representative spectra are thus chosen as the ones with I_D/I_G ratio closer to their average within the same sample. The I_D/I_G ratios are also included for the presented spectra. The results show that no detectable differences are introduced by laser-scribing the screen-printed electrodes.

In addition, the spectra show two more bands at higher Raman shifts, namely the 2D-band at 2718 cm^{-1} and the combined overtone of the D-band and G-band at 2936 cm^{-1} (both second-order bands) [28]. The 2D-band is the overtone of the D-band and is associated to a double-resonance process, which reveals layered carbon. Thus, a second figure of merit that can be used to evaluate the quality of the films is the I_{2D}/I_G intensity ratio [29]. Here, also no major changes can be detected on such parameter due to the use of the laser.

Fig. 21 shows the results for films produced with K-bar. As already demonstrated in previous sections, craters are easily identified, and so it was possible to collect spectra at the very centre of the craters and at their periphery. There seems to be an increase of the average I_D/I_G ratio in the periphery of craters in LS electrodes when compared to NLS ones (0.90 to 0.99) as the laser ablation may result in the introduction of extra defects. However, the major difference is detected when probing the inner region of the craters, where the 2D band seems to have a considerable increase. Here, the I_D/I_G ratio is similar to the periphery region, and corresponds to 0.97, while a clear decrease of the full width at half maximum (FWHM) of the D-band between periphery and inner crater regions is also observed (99.0 vs 81.6 cm^{-1}). The average I_{2D}/I_G intensities ratio for the craters in the LS electrodes is 0.25 and 0.14 for the inner and periphery areas of the craters, respectively, while for NLS it is of 0.12.

A higher intensity D-band reveals that sp2 bonds may be broken and more sp3 bonds are present when compared to unirradiated samples. Although small, differences between the intensity ratio I_D/I_G of processed and unprocessed samples are still noticeable. It should be highlighted that the original intensity ratio is already characteristic of a defective carbon structure that appears to worsen when activated carbon-based films are laser-irradiated under air. Since the samples were processed under such experimental conditions, structural and chemical defects (originated from oxide species) may still be created during laser ablation and partial film heating [29]. Once defects are present and/or the material is partially oxidized, a portion of the carbon atoms are sp3-bonded and the rise of I_D/I_G can be seen. However, the transition from sp2 to sp3 bonds can lead to a maximum of the I_D/I_G ratio before experiencing a drop [30]. The larger differences are detected between unprocessed samples and the inner region of the ablated craters where both D-band and 2D-band intensities seem to increase, with emphasis on the last one. It can be attributed to the fact that the laser ablation can cause removal of several carbon layers, leading to a clear higher 2D-band signal, and subsequent edge defects exposure.

Raman spectroscopy allows a more localized (spot size of ca. 1 µm

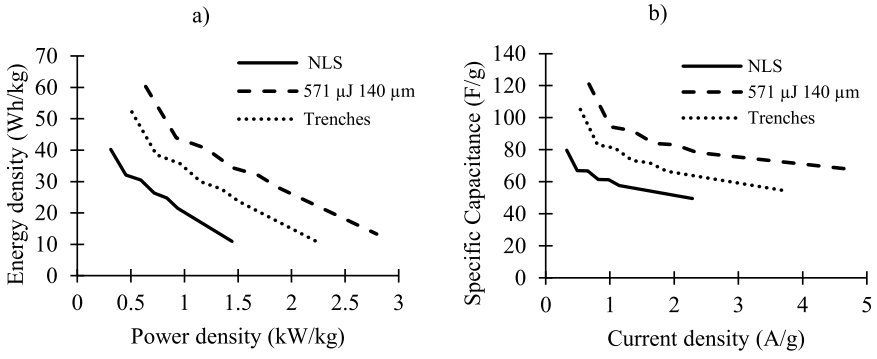


Fig. 17. Ragone plots (a) and rate capability (b) obtained for non laser-scribed (NLS) and for laser-scribed electrodes in 0.2 M tetrabutylammonium perchlorate (in acetonitrile).

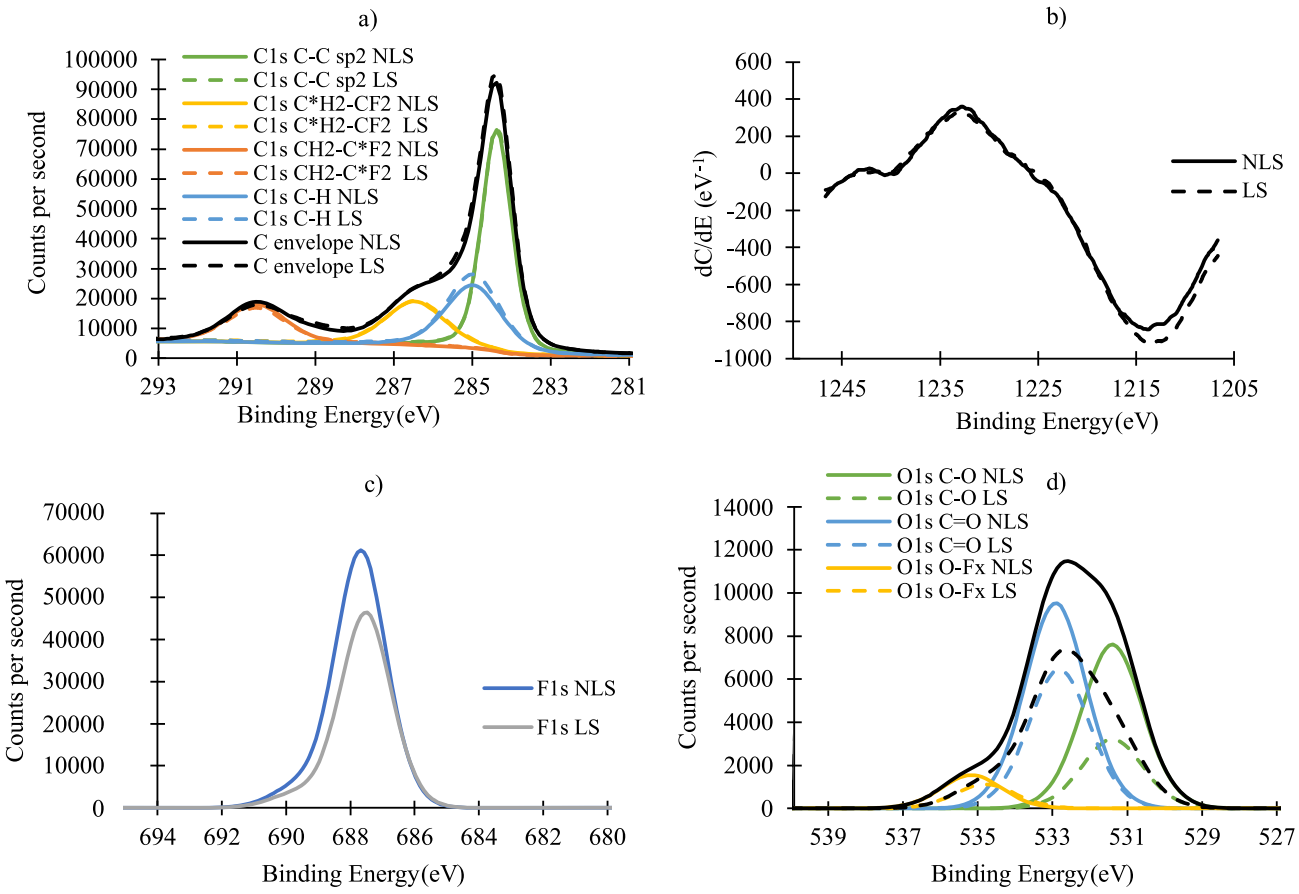


Fig. 18. Comparison of XPS results obtained for non laser-scribed (NLS) and for laser-scribed (LS) electrodes (K-bar set) with a pulse energy of 314 μJ and a spacing of 100 μm: (a) C1s peaks, (b) Differentiated CKL1 peaks (Auger). The D parameter is 18.9 for NLS and 19.4 for LS, (c) F1s peaks and (d) O1s peaks. The C/O ratio was found to be 21.8 for NLS and 19.9 for LS.

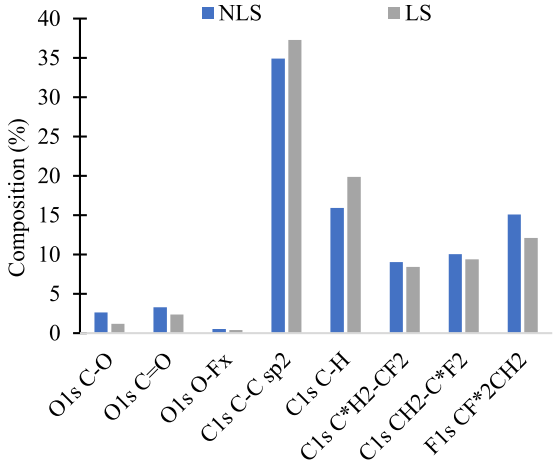


Fig. 19. Relative abundance of different chemical bonds, estimated by XPS, for non laser-scribed (NLS) and for laser-scribed (LS) electrodes (K-bar set). Laser parameters were 314 μJ laser pulse energy and 100 μm interchannel spacing.

diameter) and deeper surface analysis when compared to XPS, showing that chemistry of regions inside craters and craters periphery seem to be rather different for samples produced with K-bar. Although significant changes were detected with the Raman when probing the surface of these samples, the detected increase of the D parameter in the XPS results due to laser-scribing cannot be reinforced with the Raman results since a higher degree of graphitization was not verified when compared

Table 4
Binding energies and FWHM of each peak.

	Binding Energy (eV)		FWHM (eV)	
	NLS	LS	NLS	LS
O1s C—O	531.4	531.4	1.9	1.9
O1s C = O	532.9	532.8	1.9	1.9
O1s O-Fx	535.2	534.8	1.9	1.9
C1s C—C sp2	284.4	284.4	1.1	1.0
C1s C*H2-CF2	286.8	286.8	1.7	1.7
C1s CH2-C*F2	290.7	290.7	1.7	1.7
F1s CF*2CH2	687.7	687.5	1.9	1.9
C1s C—H	285.2	285.2	1.6	1.7

to as-produced samples. Also, the contribution from the sample upper surface levels to the XPS signal is expected to be higher when compared to the contribution from the inner regions of the craters. Given that the surface area unaffected by the laser is also larger than the one that suffered some degree of chemistry change due to the direct incidence of the laser beam (i.e., mostly craters' periphery), it is expected that the XPS signal has a larger contribution from unprocessed areas and thus, the verified increase in the D parameter may be a result of the shallow graphitization (few surface nanometres) in areas that do not belong to craters periphery or even a potential variability in surface chemistry between different surface areas of as-produced electrodes.

4. Conclusions

Two sets of thick carbon-based supercapacitor electrodes were laser-

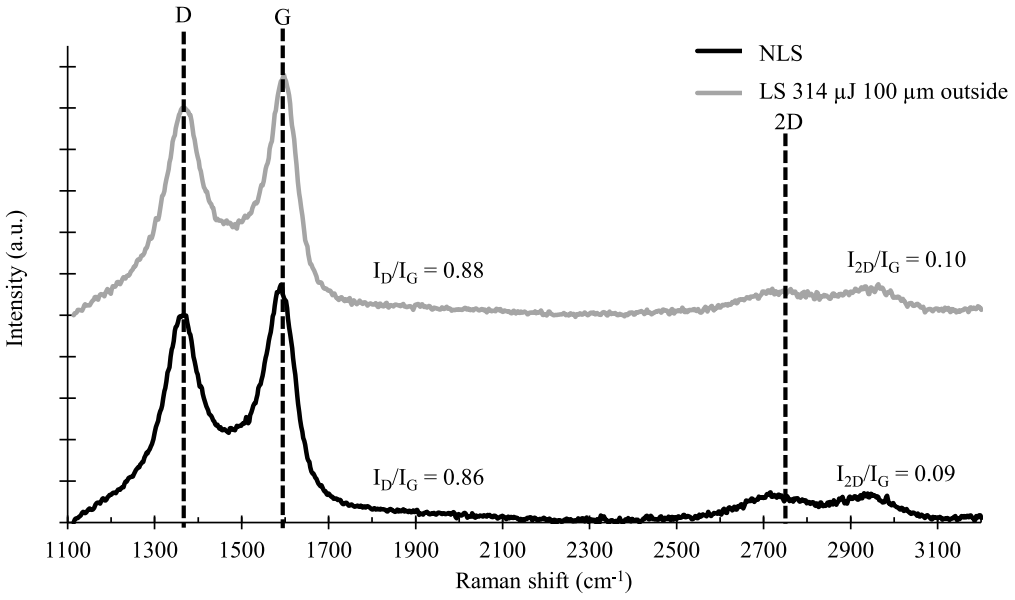


Fig. 20. Raman spectra for non laser-scribed (NLS) and laser-scribed (LS) electrodes (SP set).

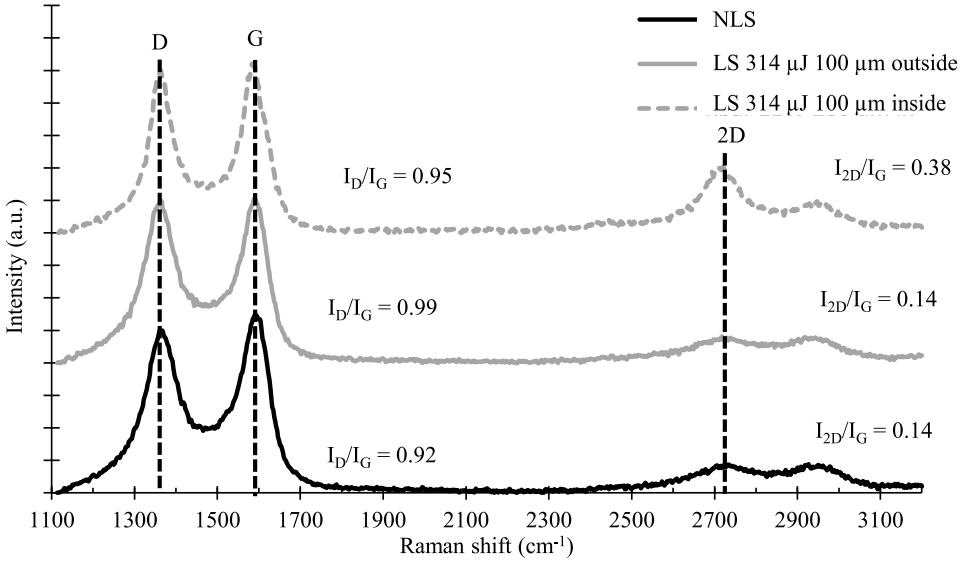


Fig. 21. Raman spectra of non laser-scribed (NLS) and laser-scribed (LS) electrodes (K set).

scribed with nine different sets of parameters (combinations of three pulse energies and three interchannel distances) and their respective performances were compared to those of non-laser-scribed electrodes. The first set of electrodes were screen-printed (SP electrodes) and already possessed a high macroporosity, even before laser-scribing whilst the second set (electrodes K) had more compact films. However, even for SP electrodes, all the laser-scribing conditions resulted, on average, in improved rate capabilities. Amongst the best results, the Ragone plots obtained for the electrodes laser-scribed at 314 µJ with an interchannel distance of 100 µm had a slope of only −4.1 Wh/kW, compared to −8.2 Wh/kW obtained for the non-laser-scribed electrodes, without any apparent damage to the cyclability. We attribute this improvement to a facilitated ionic diffusion (Warburg coefficient decreased from 15.1 $\Omega/\sqrt{s}$ to 12.4 $\Omega/\sqrt{s}$) and consequent decrease in the electrode's internal resistance, which leads to a lower potential drop. Since this enables wider potential ranges at high current densities, the energy density increases because it is proportional to the square of the operational ΔV. However, at low rates, the energy density is negatively affected because the overall specific capacitance of the laser-scribed electrodes is ca. 30% lower. Despite having a less impressive improvement in the rate capability, the electrodes processed at 314 µJ with an interchannel distance of 140 µm have their energy density starting to exceed that of non-laser-scribed electrodes at lower power densities (>250 W/kg). For laser-scribed K electrodes, the slope of the Ragone plot only decreased by ca. 20% in the best set of conditions. However, for both sets of electrodes, a negative trade-off is observed: laser processed electrodes seem to have a lower specific capacitance. This might be caused by the entrapment of debris in the laser-drilled holes, which could lead to the overestimation of the active mass. Moreover, XPS analysis suggests that this may also be explained by the decrease in the oxygen functionalities and by its impact on the electrodes' wettability. On the other hand, for electrodes tested in an organic electrolyte (TBAP in acetonitrile), the specific capacitance at 2 A/g was up to 66% higher for laser-scribed electrodes and an energy density of 13 Wh/kg was

achieved even at 2.8 kW/kg.

Declaration of Competing Interest

The authors declare that they have no known competing financial interests or personal relationships that could have appeared to influence the work reported in this paper.

Acknowledgments

This work was funded by the Portuguese Fundação para a Ciência e a Tecnologia (FCT) I.P./MCTES through national funds (PIDDAC) – UIDB/50019/2020 and PD/BD/128169/2016 and also by the UK EPSRC JUICED Hub project EP/R023662/1. The authors acknowledge as well the support from António J. S. Fernandes with Raman spectroscopy measurements and the use of facilities supported by the projects i3N, UIDB/50025/2020, UIDP/50025/2020 & LA/P/0037/2020, financed by national funds through the FCT/MCTES. The authors also thank the use of facilities at CICECO-Aveiro Institute of Materials with project references UIDB/50011/2020, UIDP/50011/2020 & LA/P/0006/2020, financed by national funds through the FCT/MEC (PIDDAC). Finally, the authors are grateful to Filipe Serra, to Professor Jorge Correia, to Professor Ana Viana and to Daniel Santos for the fruitful discussions and for lab supplies.

References

[1] S. Huang, X. Zhu, S. Sarkar, Y. Zhao, Challenges and opportunities for supercapacitors, APL Mater. 7 (2019), https://doi.org/10.1063/1.5116146.
[2] A. González, E. Goikolea, J.A. Barrena, R. Mysyk, Review on supercapacitors: technologies and materials, Renew. Sustain. Energy Rev. 58 (2016) 1189–1206, https://doi.org/10.1016/j.rser.2015.12.249.
[3] M.A.A. Mohd Abdah, N.H.N. Azman, S. Kulandaivalu, Y. Sulaiman, Review of the use of transition-metal-oxide and conducting polymer-based fibres for high-performance supercapacitors, Mater. Des. 186 (2020), 108199, https://doi.org/10.1016/j.matdes.2019.108199.
[4] T. Brousse, O. Crosnier, D. Bélanger, J.W. Long, Capacitive and Pseudocapacitive Electrodes for Electrochemical Capacitors and Hybrid Devices, in: met. Oxides Supercapacitors, Elsevier Inc., 2017: pp. 1–24. https://doi.org/10.1016/b978-0-12-810464-4.00001-2.
[5] C. Schütter, S. Pohlmann, A. Balducci, Industrial requirements of materials for electrical double layer capacitors: impact on current and future applications, Adv. Energy Mater. 9 (2019) 1–11, https://doi.org/10.1002/aenm.201900334.
[6] L. Chang, Y.H. Hu, Breakthroughs in designing commercial-level mass-loading graphene electrodes for electrochemical double-layer capacitors, Matter 1 (2019) 596–620, https://doi.org/10.1016/j.matt.2019.06.016.
[7] V.V.N. Obreja, Supercapacitors specialities - materials review, AIP Conf. Proc. 1597 (2014) 98–120, https://doi.org/10.1063/1.4878482.
[8] L. Chang, W. Wei, K. Sun, Y.H. Hu, 3D flower-structured graphene from CO_2 for supercapacitors with ultrahigh areal capacitance at high current density, J. Mater. Chem. A. 3 (2015) 10183–10187, https://doi.org/10.1039/c5ta01055a.
[9] Y. Dong, J. Zhu, Q. Li, S. Zhang, H. Song, D. Jia, Carbon materials for high mass-loading supercapacitors: filling the gap between new materials and practical applications, J. Mater. Chem. A 8 (2020) 21930–21946, https://doi.org/10.1039/d0ta08265a.
[10] A.H.Ab. Rahim, N. Ramli, A.N. Nordin, M.F.Abd. Wahab, Supercapacitor performance with activated carbon and graphene nanoplatelets composite electrodes, and insights from the equivalent circuit model, Carbon Trends 5 (2021), 100101, https://doi.org/10.1016/j.cartre.2021.100101.
[11] T. Liu, F. Zhang, Y. Song, Y. Li, Revitalizing carbon supercapacitor electrodes with hierarchical porous structures, J. Mater. Chem. A 5 (2017) 17705–17733, https://doi.org/10.1039/c7ta05646j.
[12] F. Béguin, V. Presser, A. Balducci, E. Frackowiak, Carbons and electrolytes for advanced supercapacitors, Adv. Mater. 26 (2014) 2219–2251, https://doi.org/10.1002/adma.201304137.
[13] Y. Korenblit, M. Rose, E. Kockrick, L. Borchardt, A. Kvit, S. Kaskel, G. Yushin, High-rate electrochemical capacitors based on ordered mesoporous silicon carbide-derived carbon, ACS Nano 4 (2010) 1337–1344, https://doi.org/10.1021/nn901825y.
[14] Y. Zhang, S. Yu, G. Lou, Y. Shen, H. Chen, Z. Shen, S. Zhao, J. Zhang, S. Chai, Q. Zou, Review of macroporous materials as electrochemical supercapacitor electrodes, J. Mater. Sci. 52 (2017) 11201–11228, https://doi.org/10.1007/s10853-017-0955-3.
[15] J.Y. Hwang, M. Li, M.F. El-Kady, R.B. Kaner, Next-generation activated carbon supercapacitors: a simple step in electrode processing leads to remarkable gains in energy density, Adv. Funct. Mater. 27 (2016) 1–11, https://doi.org/10.1002/adfm.201605745.
[16] R. Vedalakshmi, V. Saraswathy, H.W. Song, N. Palaniswamy, Determination of diffusion coefficient of chloride in concrete using Warburg diffusion coefficient, Corros. Sci. 51 (2009) 1299–1307, https://doi.org/10.1016/j.corsci.2009.03.017.
[17] R. Poprawe, Tailored Light 2, Springer Berlin Heidelberg, Berlin, Heidelberg, 2011, https://doi.org/10.1007/978-3-642-01237-2.
[18] E. Cappelli, C. Scilletta, S. Orlando, V. Valentini, M. Servidori, Laser annealing of amorphous carbon films, Appl. Surf. Sci. 255 (2009) 5620–5625, https://doi.org/10.1016/j.apsusc.2008.10.062.
[19] G. Speranza, N. Laidani, Measurement of the relative abundance of sp2 and sp3 hybridised atoms in carbon based materials by XPS: a critical approach, Part I Diam. Relat. Mater. 13 (2004) 445–450, https://doi.org/10.1016/j.diamond.2003.11.077.
[20] S.T. Jackson, R.G. Nuzzo, Determining hybridization differences for amorphous carbon from the XPS C 1s envelope, Appl. Surf. Sci. 90 (1995) 195–203, https://doi.org/10.1016/0169-4332(95)00079-8.
[21] D.J. Morgan, Comments on the XPS analysis of carbon materials, C 7 (2021) 51. https://doi.org/10.3390/c7030051.
[22] A.J. Barlow, S. Popescu, K. Artyushkova, O. Scott, N. Sano, J. Hedley, P. J. Cumpson, Chemically specific identification of carbon in XPS imaging using Multivariate Auger Feature Imaging (MAFI), Carbon N. Y. 107 (2016) 190–197, https://doi.org/10.1016/j.carbon.2016.05.073.
[23] A.F. Alba, J. Totoricaguena-Gorriño, L. Campos-Arias, N. Peřinka, L. Ruiz-Rubio, J. L. Vilas-Vilela, S. Lanceros-Méndez, F.J. del Campo, Laser-induced highly oriented pyrolytic graphite for high-performance screen-printed electrodes, Mater. Adv. 2 (2021) 5912–5921, https://doi.org/10.1039/d1ma00582k.
[24] M. Seredych, D. Hulicova-Jurcakova, G.Q. Lu, T.J. Bandosz, Surface functional groups of carbons and the effects of their chemical character, density and accessibility to ions on electrochemical performance, Carbon N. Y. 46 (2008) 1475–1488, https://doi.org/10.1016/j.carbon.2008.06.027.
[25] Y.F. Chen, T. Zhang, M. Tang, D. Xie, Q. Long, C.Y. Li, The effect of high-current pulsed electron beam modification on the surface wetting property of polyamide 6, E-Polymers 17 (2017) 23–29, https://doi.org/10.1515/epoly-2016-0078.
[26] S. Ghosh, S. Barg, S.M. Jeong, K. Ostrikov, Heteroatom-doped and oxygen-functionalized nanocarbons for high-performance supercapacitors, Adv. Energy Mater. 10 (2020), https://doi.org/10.1002/aenm.202001239.
[27] A. Reyhani, A. Nozad Golikand, S.Z. Mortazavi, L. Irannejad, A.Z. Moshfegh, The effects of multi-walled carbon nanotubes graphitization treated with different atmospheres and electrolyte temperatures on electrochemical hydrogen storage, Electrochim. Acta 55 (2010) 4700–4705, https://doi.org/10.1016/j.electacta.2010.03.061.
[28] B. Ma, R.D. Rodriguez, A. Ruban, S. Pavlov, E. Sheremet, The correlation between electrical conductivity and second-order Raman modes of laser-reduced graphene oxide, Phys. Chem. Chem. Phys. 21 (2019) 10125–10134, https://doi.org/10.1039/c9cp00093c.
[29] V. Romano, L. Torrisi, M. Cutroneo, V. Havranek, G. D'Angelo, Raman investigation of laser-induced structural defects of graphite oxide films, EPJ Web Conf. 167 (2018) 2–6, https://doi.org/10.1051/epjconf/201816704011.
[30] A.C. Ferrari, J. Robertson, Interpretation of Raman spectra of disordered and amorphous carbon, Phys. Rev. B 61 (2000) 14095–14107, https://doi.org/10.1103/PhysRevB.61.14095.



https://dspace.org/

The impact of laser-scribing carbon-based supercapacitor electrodes

Baptista, Joana M.; Gaspar, Guilherme; Wijayantha, Upul K. G.; Lobato, Killian

2022-06-06
Elsevier
https://doi.org/10.1016/j.apsadv.2022.100262
Baptista JM, Gaspar G, Wijayantha KGU, Lobato K. (2022) The impact of laser-scribing carbon-based supercapacitor electrodes. Applied Surface Science Advances, Volume 10, August 2022, Article number 100262

Downloaded from a DSpace repository. https://dspace.org/